Supporting Information

Kinetic origins of the metastable zone width in

the manganese oxide Pourbaix diagram

Bor-Rong Chen[1], Wenhao Sun[2,3], Daniil A. Kitchaev[5], Kevin H. Stone[1], Ryan C. Davis[1],
Gerbrand Ceder[2,4], Laura T. Schelhas[6,7], Michael F. Toney[1,8]

[1]Stanford Synchrotron Light Source, SLAC National Accelerator Laboratory, Menlo Park, CA 94025, USA
[2]Materials Science Division, Lawrence Berkeley National Laboratory, Berkeley, CA 94720, USA
[3]Department of Materials Science and Engineering, University of Michigan, Ann Arbor, Michigan, 48109, USA
[4] Department of Materials Science and Engineering, UC Berkeley, Berkeley, CA 94720, USA
[5]Materials Department, UC Santa Barbara, Santa Barbara, CA 93117, USA.
[6]Applied Energy Division, SLAC National Accelerator Laboratory, Menlo Park, CA 94025, USA
[7]National Renewable Energy Laboratory, Golden, CO 80401, USA
[8]Department of Chemical and Biological Engineering, University of Colorado Boulder, Boulder, CO 80309, USA

Table of Contents

Supporting Information 1. Sample _p_H and ORP conditions

Table S1. Summary of the sample conditions with varying _p_H values. The _p_H and ORP were measured using a _p_H/ORP meter (VWR Traceable) immediately after the reaction solution was thoroughly mixed. The concentration of Mn in the solution was kept at 0.2 M.

*ORP: oxidation reduction potential

Concentration of HNO_3	_p_H	ORP (meV)*
1 M	0.5	1280
0.2 M	1.1	1220
0.1 M	1.3	1200
0.05 M	1.7	1170
0.04 M	1.8	1170
0.02 M	2.0	1160
0.005 M	2.6	1100

Supporting Information 2. Set up for the *in situ* wide-angle X-ray scattering (WAXS) and X-ray absorption spectroscopy (XAS)

WAXS: WAXS data were collected at Beamline 11-3 at the Stanford Synchrotron Radiation Lightsource (SSRL) with an incident wavelength of 0.9744 Å. A custom-build sample holder/heater, as shown in Figure S1(a), was used to heat the reactors. The heat is applied to the reactor by using an Omega Lux air heater. An external variac was used to control the temperature of the reactor. A Kimble 2502 glass capillary (0.1mm wall thickness, 1 mm diameter, and 75mm length) was used as the hydrothermal vessel. To protect the 2D detector in the event of capillary failure during the reaction, the sample holder was covered by a layer of Kapton film. To avoid sudden increase or decrease of scattering intensity due to random movements of crystalline MnO_2 and air bubbles in the reactor, the reactor was translated in its longitudinal direction for $\pm$ 1 mm during the measurements.

XAS: The same custom-build sample holder/heater were used in the XAS measurements, as shown in Figure S1(b). The XAS data were taken at Beamline 4-1 at SSRL. The XAS experiments were carried out at Mn K edge (6539 eV). A capillary tube with a thinner wall thickness were used (Charles Supper, 0.01 mm wall thickness, 0.7 mm diameter, and 80 mm length) to avoid X-ray self-absorption. The energy range of the XAS scan was from 6310 to approximately 7000 eV for the *p*H 0.5 and *p*H 1.1 samples. For the *p*H 2.6 samples, the ranged used was 6310 to 6800 eV. ATHENA software package was used for data processing and linear combination fitting (LCF) over the range of -20 – +30 eV with respect to the Mn K edge.
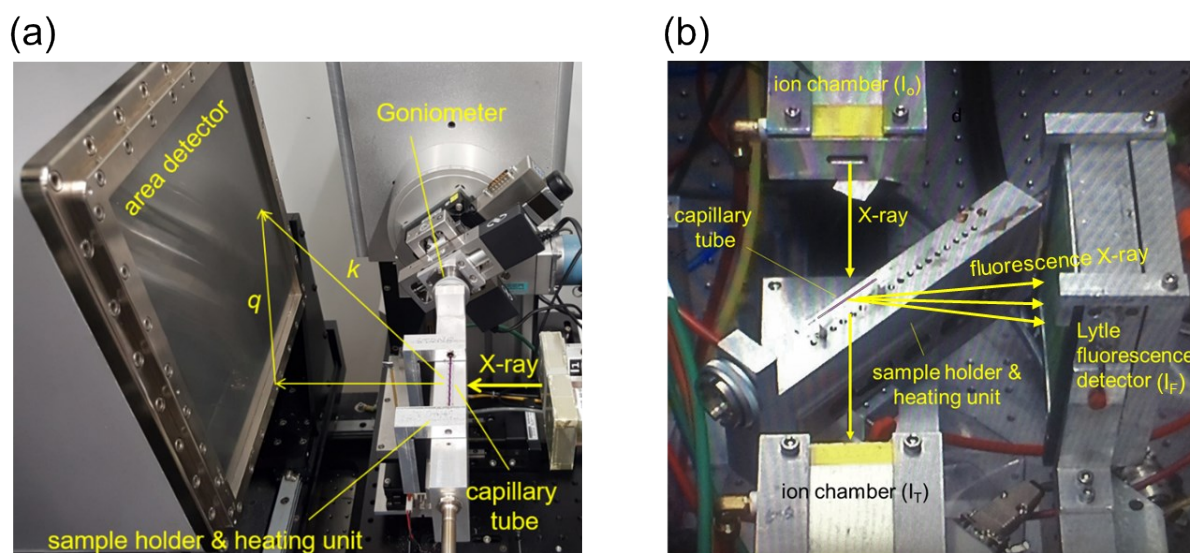
Figure S1. The set-up of in-situ X-ray measurements of MnO_2 hydrothermal synthesis. (a) WAXS at SSRL beamline 11-3 (further details can be referred to our previous publication[1]), and (b) XAS at SSRL beamline 4-1. Different parts of the instruments are marked accordingly.

Supporting Information 3. Onset time of δ'-MnO$_2$ crystallization at varying pH

Table S2. Summary of the WAXS onset time at different pH and temperatures. To gain a better signal to noise ratio while determining the onset of MnO$_2$ crystallization, every three scattering profiles were averaged. For the pH 0.5 and pH 1.1 data sets at 160 °C, the crystallization occurs quickly at the first few minutes and the scattering profiles for these two conditions were not averaged to gain better time resolution.

| pH	δ'-MnO$_2$ onset time at 160 °C (min)	δ'-MnO$_2$ onset time at 120 °C (min)
0.5	5	26
1.1	6	29
1.3	20	32
1.7	23	35
1.8	29	-
2.0	> 572 min ~ 9.6 hr	> 578 min ~ 9.6 hr
2.6	> 539 min ~8.9 hr	> 908 min ~15 hr
	> 21 hr[*]	> 90 hr ~3.75 days[**]

[*]data obtained by performing parallel *ex situ* hydrothermal synthesis using the same capillary tube and heated in a conventional oven, then measured using same set up as the *in situ* WAXS experiments.

 [**]data obtained by performing parallel *ex situ* hydrothermal synthesis using autoclaves, showing no visually observable precipitation.
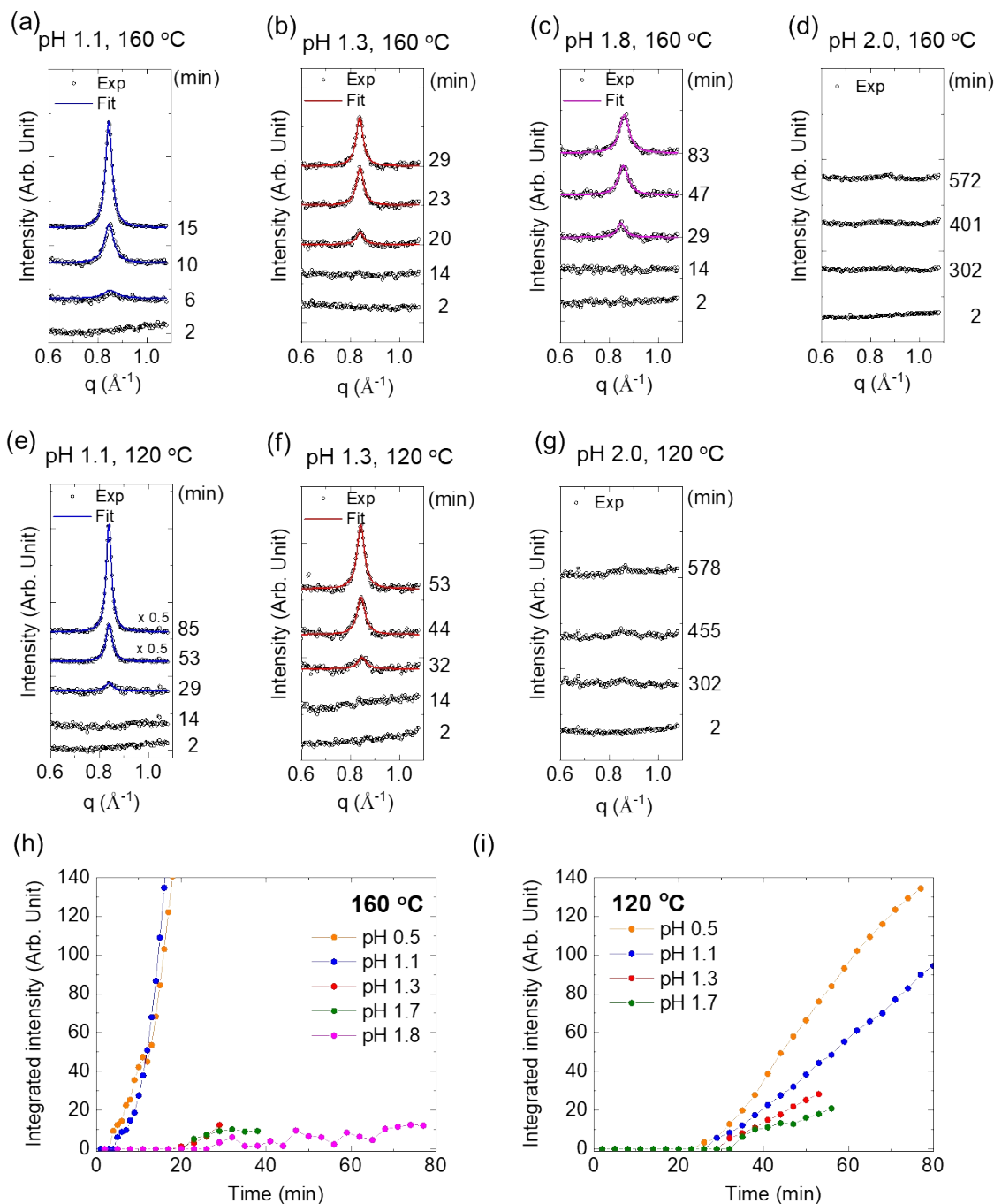
Figure S2. Evolution of the δ'-MnO$_2$ (200) peak with representative time and *p*H values at 160 °C (a-d) and 120 °C (e-g). (d-e) Integrated intensity of the (200) scattering peak as a function of time. The figures show the *p*H values that are not presented in the manuscript and the intensity evolution from 40 min to 80 min.

Supporting Information 4. Full WAXS profiles during δ'-MnO₂ crystallization
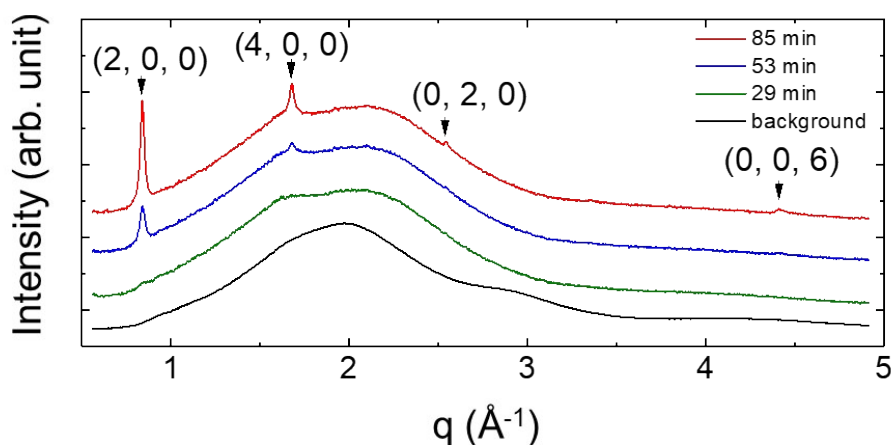
Figure S3. Full 1D WAXS profiles of representative data points (29, 53, and 85 min) during the δ'-MnO₂ crystallization at *p*H 1.1. In Figure 2 of the manuscript, only the (200) scattering peak is shown. The four diffraction peaks are representative for the δ'-MnO₂, as discussed in our previous publication[1]. The broad peak around q = 1.5–2.5 Å⁻¹ is caused by imperfect background removal. Note that the incomplete removal of the background is caused by the variation of capillary wall thickness due to the ± 1 mm translation along the capillary tube, as well as the variation of the composition in the aqueous phase as MnO₂ crystallizes. Therefore, the background profile (scattering profile at t = 0 min, marked as the black line in the figure) was multiplied with a constant less than 1 before subtraction to avoid over-subtraction.

Supporting Information 5. X-ray absorption spectrum at the endpoint of *in situ* reaction

The X-ray absorption spectrum of the endpoint scans (pH 0.5, 63 min and pH 1.1, 85 min) are compared to the dry δ'-MnO$_2$ reference to confirm that the structure features are the same. Figure S4 (a-b) shows the X-ray absorption near edge spectra (XANES), and the corresponding extended X-ray absorption fine structure (EXAFS) are shown in Figure S4 (c-d). In both of the cases, the end point XANES spectrum show features of the dry δ'-MnO$_2$ reference. In the EXAFS results, the two peaks representing the Mn–O (~1.9 Å) and Mn–Mn (~ 2.8 Å) nearest-neighbors in the δ'-MnO$_2$ are clearly observed. The position of these two peaks are consistent with the dry δ'-MnO$_2$ reference.
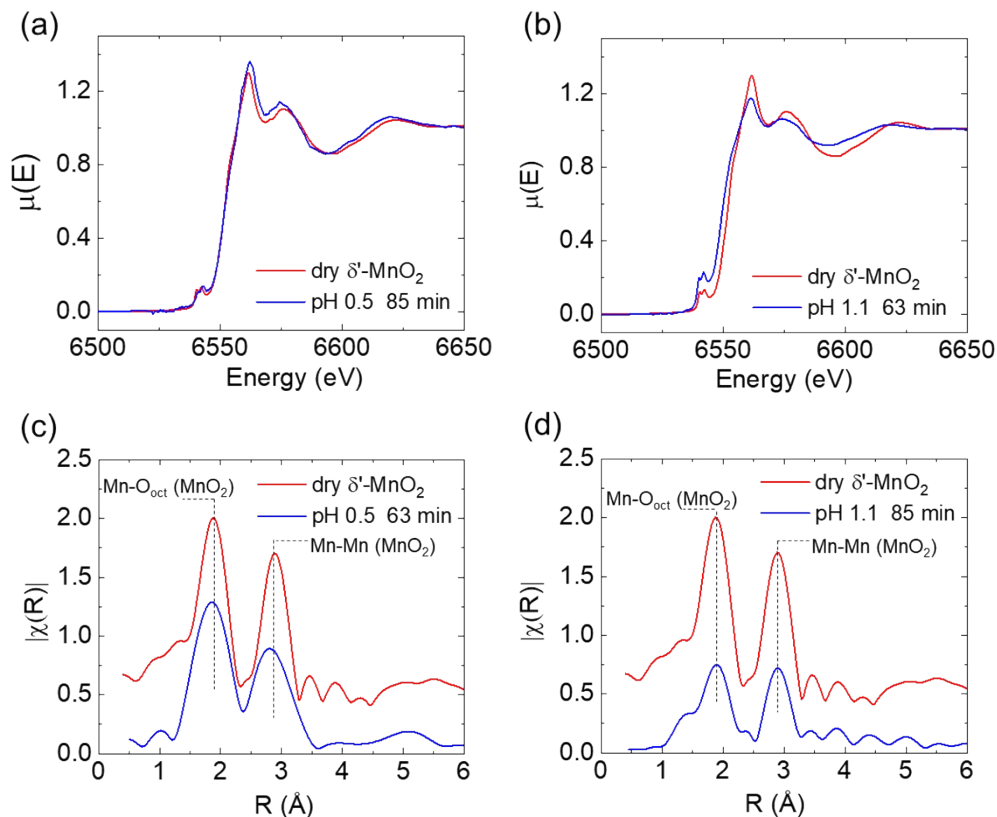
Figure S4. Comparison between the XANES and EXAFS of the endpoint spectrum and dry δ'-MnO$_2$ reference. (a) XANES of pH 0.5 at 63 min, (b) XANES of pH 1.1 at 85 min, (c) EXAFS of pH 0.5 at 63 min, and (d) EXAFS of pH 1.1 at 85 min. Note that the lower quality of the EXAFS of pH 0.5 at 63 min is due to the shorter data range.

Supporting Information 6. *In situ* **EXAFS of the δ'-MnO₂ crystallization at *p*H 1.1**
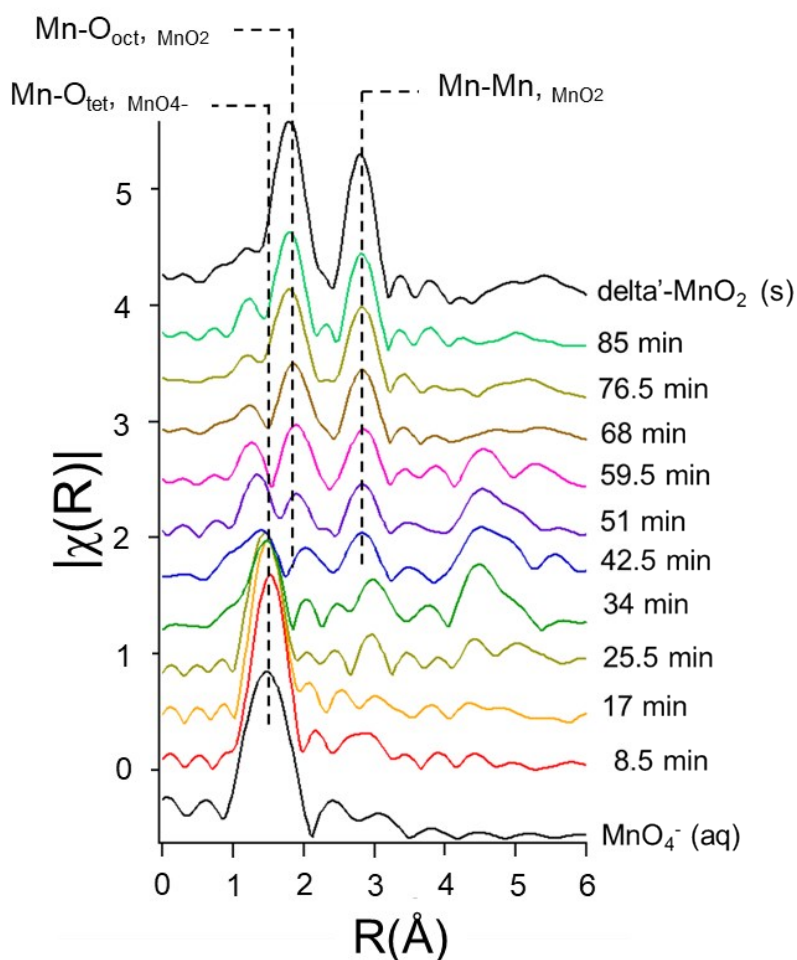

Figure S5. Fourier transformed EXAFS of the (*p*H 1.1, 120 °C) sample as a function of reaction time. The peaks characteristic to the MnO_4^- (aq) and dry δ'-MnO₂ (s) (black traces) are marked, showing the gradual transition from MnO_4^- to δ'-MnO₂. The positions of the Mn-O$_{tet}$ and Mn-O$_{oct}$ peaks shift during the transition period (25.5 – 59.5 min). This shift could be explained by the re-organization of isolated Mn$_{tet}$ to the Mn$_{tet}$-Mn$_{oct}$ complexes, then to extended MnO₂ crystals, as shown in Figure 7(a) in the manuscript. An alternative explanation is that the continuous increase in bond length reflects the reduction of the MnO$_x$ complexes, since more reduced Mn states correspond to longer Mn-O bond lengths.

Supporting Information 7. Linear combination fitting results of Mn XANES

The atomic fractions of tetrahedrally-coordinated Mn (Mn$_{tet}$) and octahedrally-coordinated Mn (Mn$_{oct}$) during the transition process were calculated using linear combination analysis. The two end member components used in the fitting are the room temperature spectra of individual pathways and the dry δ'-MnO$_2$ powder. In order to take the solvation environment in the in-situ reaction into consideration, the endpoint spectra of pH 0.5 (63 min) and pH 1.1 (85 min) were also used when performing the linear combination analysis. The two sets of fitting results are compared in Figure S5, showing consistency between each other.
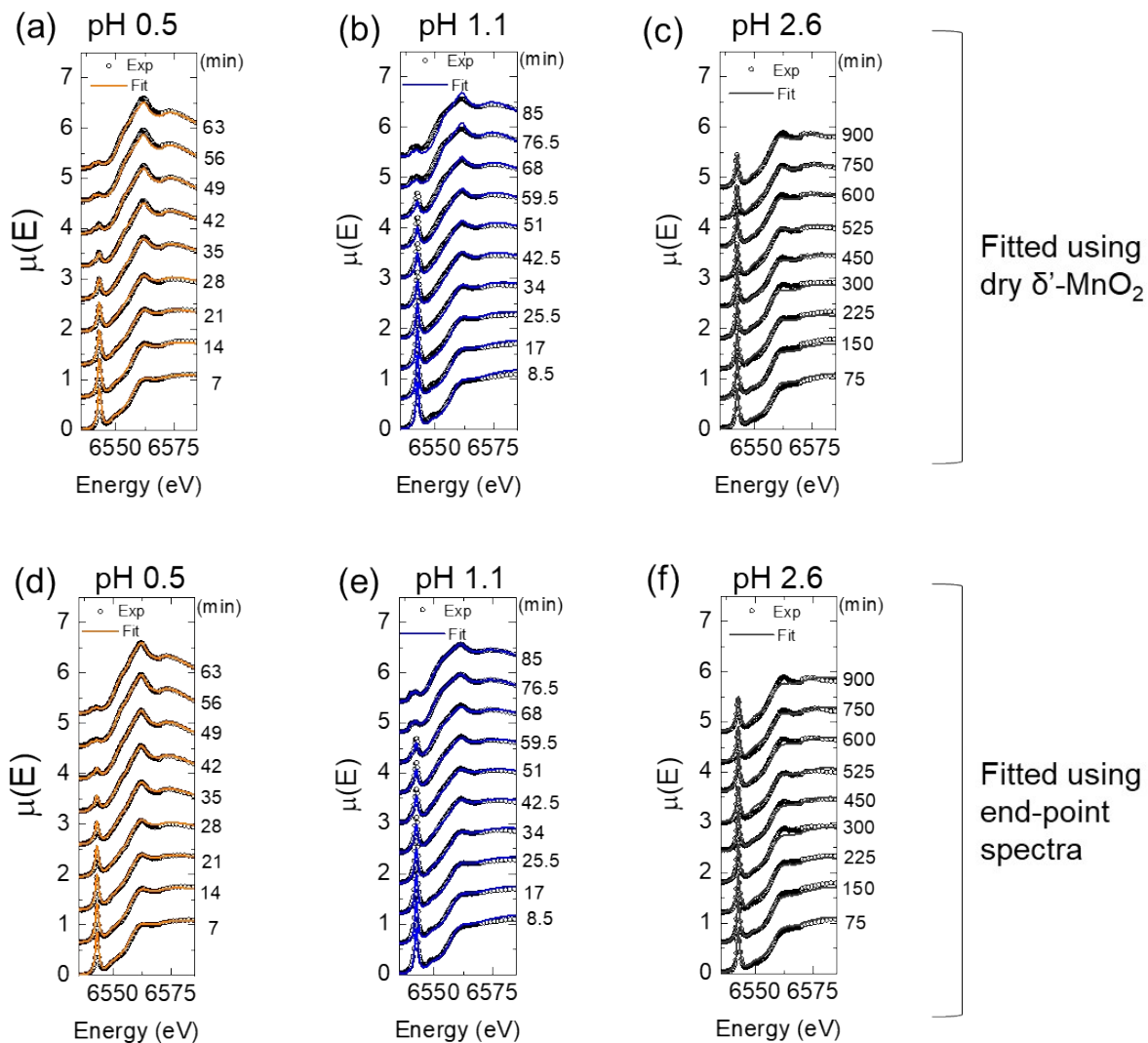
Figure S6. The Mn K edge XANES of MnO$_2$ crystallization as a function of reaction time (open dot) and the linear combination fitting results (solid line) at 120 °C. (a-c) Fit using dry δ'-MnO$_2$. (d-f) Fitted data using the endpoint spectra.

Supporting Information 8. Half-life of Mn$_{tet}$ obtained by XANES

Table S3. Summary of the half-life of Mn$_{tet}$ obtained by XANES at different pH values.

*estimated by extrapolating the linear trend of Mn$_{tet}$ fraction versus time because the half-life is outside of the measurement time

pH	XANES onset time at 120 °C (min)
0.5	28 ± 4
1.1	46 ± 5
2.6	$939 \pm 4^*$

Supporting Information 9. The full Mn Pourbaix diagram
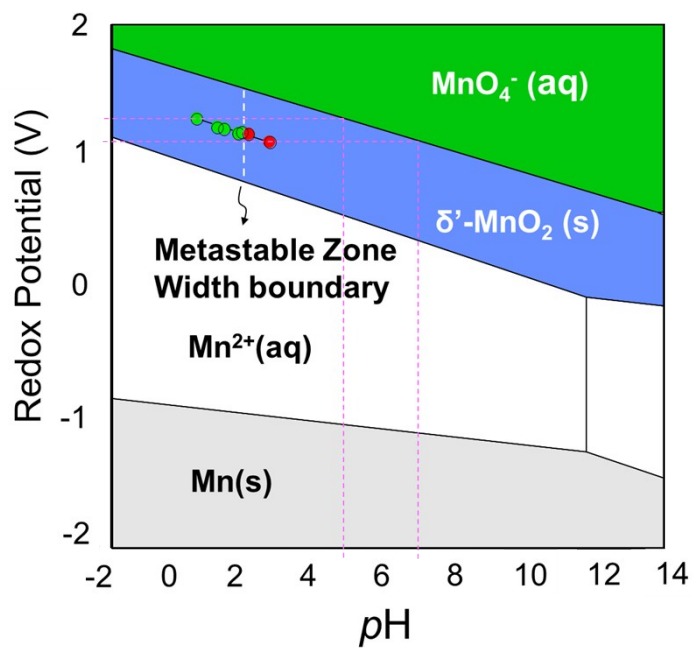

Figure S7. The full Mn Pourbaix diagram showing the MnO_4^-(aq) and δ'-MnO_2 phases specifically. The magenta lines indicate the equilibrium phase boundary between MnO_4^- and δ'-MnO_2 at the experimental conditions in this work (green and red dots). The phase boundary corresponding to E ~ +1.3 – 1.1 V is near pH ~ 5 – 7.

Supporting Information 10. Mn$_{tet}$ fraction at the onset of solid MnO$_2$

From the XANES observation results, we estimate the fraction of Mn$_{tet}$ at the onset of solid MnO$_2$ formation. Figure S8 shows linear interpolation results of the XANES data. The onset time of pH 0.5 and pH 1.1 at 120 °C are 26 min and 29 min, respectively, as measured by WAXS. The onsets correspond to a Mn$_{tet}$ fraction of 0.54 ± 0.01 and 0.66 ± 0.02, respectively.

(a)

(b)
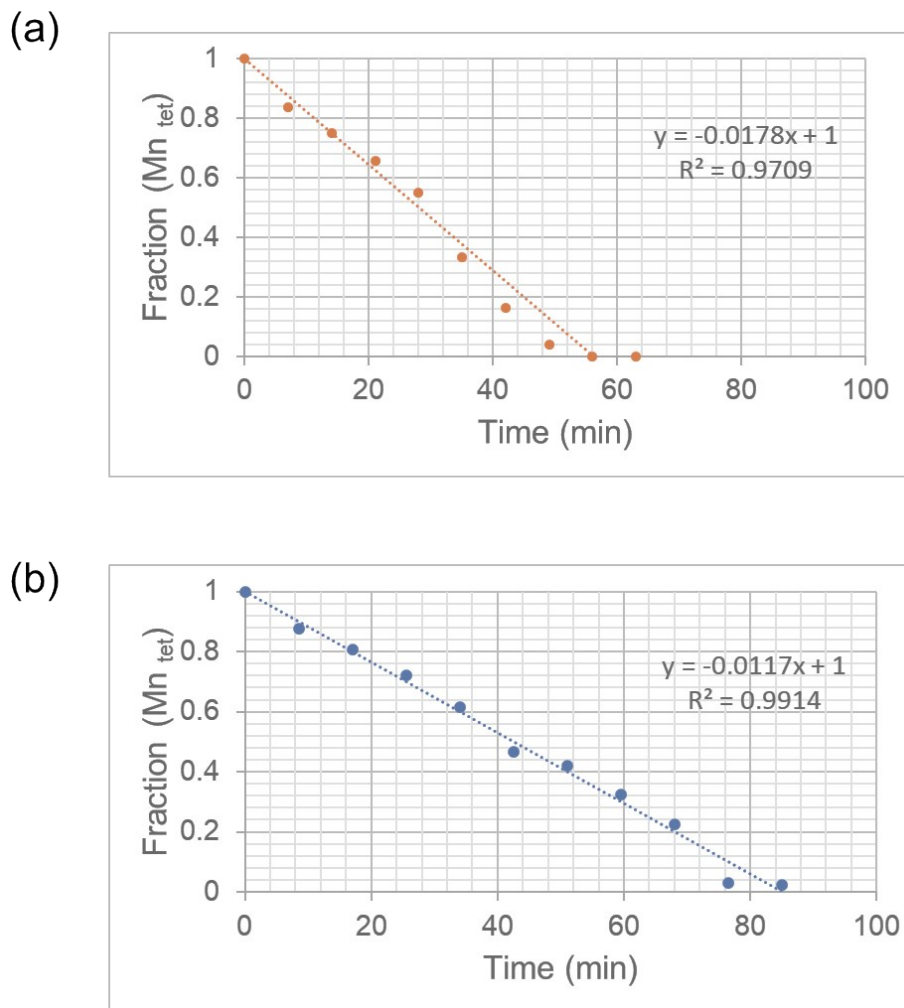
Figure S8. Linear interpolation of the Mn$_{tet}$ fraction at the solid MnO$_2$ onset time for pH 0.5 (a) and pH 1.1 (b) at 120 °C. The linear regression equation and the R^2 value are shown in the figures accordingly.

**Supporting Information 11. Thermodynamic driving force (ΔΨ) for redox-active precipitation reaction**

In general, the kinetics of a phase transformation can be limited by three mechanisms: 1) reactant diffusion, 2) crystal nucleation, or 3) crystal growth[2]. In hydrothermal synthesis, precursor transport through an aqueous media is fast, so it is reasonable to assume that precursor diffusion is not the kinetic limitation for non-equilibrium crystallization phenomena. Between nucleation and crystal growth, the barrier to crystal growth is small or negligible, whereas the barrier to nucleation can be significant, especially at the low-temperatures (< 200 °C) of hydrothermal synthesis[3]. For these reasons, we can largely attribute non-equilibrium phenomena in aqueous precipitation to nucleation kinetics.

In classical nucleation theory, the critical nucleation barrier is a competition between surface energy and bulk thermodynamic driving force, and is expressed as:

$$\Delta G^* = \frac{4\,\rho^2(\eta\gamma)^3}{27\Delta G_{bulk}^2}$$

where γ is the surface energy of the nuclei, ρ is the molar volume, η is the nuclei shape factor, and ΔG_{bulk} is the bulk thermodynamic driving force for crystal formation[2]. For simple salts, such as NaCl or $CaCO_3$, the thermodynamic driving force of the crystallization is given by $\Delta G_{Bulk} = -RT \ln \sigma$. Here, σ is the degree of supersaturation and is proportional to the dissolved ion concentration divided by the solubility product constant of the solid, K_{sp}. For these simple salts, the more solute that is dissolved in solution, the greater the driving force for crystallization (ΔG_{Bulk}), and the smaller the nucleation barrier.

In a redox-active system, the thermodynamic driving force for nucleation becomes more complicated. It is not only a function of the ion concentration, but further depends on the electrochemistry of the aqueous solution, specifically, the pH and the redox potential. For example, the reduction of Mn from a highly-oxidized solution precursor, such as permanganate ion ($MnO_4^-(aq)$, Mn^{7+}), into the solid-state MnO_2 (Mn^{4+}) phase can be driven under acidic conditions, by the reaction:

$$MnO_4^-(aq) + H^+ \rightarrow MnO_2 + 0.5\ H_2O + 1.5\ O_2\ (g)$$
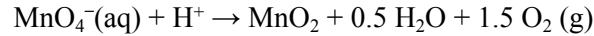
Or the reduction can be driven electrochemically, by adding a reducing agent in the reaction:

$$2H_2O + MnO_4^-(aq) + 3e^- \rightarrow MnO_2 + 4OH^-$$
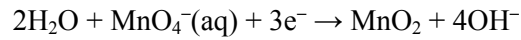
In a real redox-active precipitation reaction, the transformation of a soluble metal ion into an insoluble solid compound can be a combination of these two reactions—being driven partially by reducing agents and partially by acidic pH. This mixed reaction nature means that evaluating the thermodynamics of redox reactions by explicitly formulating the chemical reactions can be cumbersome. Previously, we derived a new expression for the free-energy of an aqueous system, where the boundary conditions are redefined in terms of redox potential (E) and pH.[4] These are the natural variables of the Pourbaix diagram, and so we named this thermodynamic potential the Pourbaix potential, $\bar{\Psi}$, which is expressed as:

$$\bar{\Psi} = \frac{1}{N_{Mn}}\left((G - N_O\mu_{H_2O}) - RT \cdot \log(10) \cdot (2N_o - N_H) \cdot pH - (2N_o - N_H + Q)E\right)$$

Here, G is the molar Gibbs free energy of a metal oxide/ion; N_M, N_O and N_H are the number of the metal, oxygen, and hydrogen atoms in the solution or precipitated oxide phase; and if the phase is an aqueous

ion, Q is the charge of the ion. We note that the Pourbaix potential is a Legendre transformation of the ΔG_{pbx} expression derived in Singh et. al.[5] reframed such that E and pH are the natural intensive variables of the thermodynamic grand potential.

Here, we compute the thermodynamic driving force ($\Delta\Psi$) between MnO_4^-(aq) to δ'-MnO_2 at the measured E and pH conditions in the very beginning of the reaction. The $\Delta\Psi$ does not change significantly between the pH conditions chosen for this experiment, as shown in Table S4.

Table S4. $\Delta\Psi$ between MnO_4^-(aq) to δ'-MnO_2 at different E and pH conditions at 120 °C

pH	Redox potential (V)	Induction Time (min, at 120 °C)	$\Delta\Psi = \Psi_{MnO4\text{-}(aq)} - \Psi_{\delta'\text{-}MnO2}$ (eV/Mn)
0.5	1.281	26	0.5371
1.1	1.215	29	0.5924
1.3	1.202	32	0.5838
1.7	1.166	35	0.5967
1.8	1.172	-	0.5549
2.0	1.161	No induction	0.5403
2.6	1.100	No induction	0.5806

References:

1. Chen, B. R. *et al.* Understanding crystallization pathways leading to manganese oxide polymorph formation. *Nat. Commun.* **9**, (2018).

2. Balluffi, R. W., Sam, A. & Craig, W. *Kinetics of Materials*. (John Wiley & Sons, 2005).

3. Tilbury, C. J. & Doherty, M. F. Modeling layered crystal growth at increasing supersaturation by connecting growth regimes. *AIChE J.* **63**, 1338–1352 (2017).

4. Sun, W., Kitchaev, D. A., Kramer, D. & Ceder, G. Non-equilibrium crystallization pathways of manganese oxides in aqueous solution. *Nat. Commun.* **10**, 573 (2019).

5. Singh, A. K. *et al.* Electrochemical Stability of Metastable Materials. *Chem. Mater.* **29**, 10159–10167 (2017).